This paper is the accepted version of the paper published on IEEE Transactions On Geoscience And Remote Sensing, Vol. 56, No. 3, March 2018

Digital Object Identifier 10.1109/TGRS.2017.2764381

The Ultra-Wideband Software Defined Microwave Radiometer (UWBRAD): Calibration, RFI Processing, and Initial Campaign Results

Mark Andrews, Joel T. Johnson, Hongkun Li, Kenneth C. Jezek[1], Alexandra Bringer, Chi-Chih Chen,
Domenic Belgiovane, Vladimir Leuski[3], Giovanni Macelloni[2], Marco Brogioni[2]
ElectroScience Laboratory, The Ohio State University, Columbus, OH
[1]Byrd Polar Research Center, The Ohio State University, Columbus, OH
[2]Institute of Applied Physics, Florence, Italy
[3]Microwave Radiometers and Antennas, Louisville, CO

***Abstract*—The Ultra-Wideband Software Defined Microwave Radiometer (UWBRAD) is a 0.5-2.0 GHz radiometer developed to probe temperatures inside ice sheets. Given the instrument's operation outside of protected portions of the spectrum, radio frequency interference (RFI) is a significant concern, and the instrument is designed to facilitate RFI detection and filtering. This document analyzes the design and operation of the radiometer, the accuracy and stability of the brightness temperatures it produces, and RFI analyses of the results acquired in its debut flight over northern Canada and Greenland.**

I. Introduction

At present several geophysical properties that characterize the dynamics of the polar ice caps can be derived only by glaciological models or measured in some points. For instance the….., This is the case of the ice sheet internal temperatures: the only measured information at present is obtained from a small number of deep ice core sites [XX epica, Ken 2015?]. Previous studies [1]-[7] have pointed out the potential of multi-frequency brightness temperature measurements from 0.5-2 GHz to obtain internal ice sheet temperature information. To this end, a project called "UWBRAD: Ultra-Wideband Software-Defined Microwave Radiometer for Ice Sheet Subsurface Temperature Sensing" financed by the NASA ESTO program was approves to demonstrate this new concept. The project foresaw the design and realization of the radiometer to be installed in an aircraft, the development of dedicated em models and retrieval techniques, the execution of an airborne campaign over Greenland. The innovative part of the experiment is the application for the first time of radiometry at ultrawideband. Because the frequency range 0.5-2 GHz is a crowded portion of the spectrum with only a small portion of the range protected for scientific radiometric measurements, UWBRAD is required to operate in the presence of significant radio frequency interference (RFI). There are three main objectives for UWBRAD: 1) to observe ice sheet brightness temperatures in the frequency range of 500-2000 MHz, 2) to identify and mitigate any radio frequency interference (RFI) through software defined algorithms in real-time and in post-processing, and 3) to determine internal sub-surface ice sheet temperatures through model based retrieval algorithms using measured brightness temperatures.

This article presents the design of the UWBRAD instrument (Section II), the results of calibration testing on the instrument (Section III), a description of the RFI algorithms used (Section IV), and the initial results (brightness temperatures and RFI statistics) of an airborne campaign conducted in Greenland in September 2016 (Section V). Additional information on ice sheet physical property measurements using UWBRAD is provided in a companion paper [8].

II. Description

The UWBRAD system is designed following the classical supereterodina scheme. The radiometer is composed of a wide bandwidth conical spiral antenna (Figs. 1 and 2), an RF frontend (Figs. 3 and 4), IF downconversion units (Figs. 4-6), and an analog to digital conversion backend and data processor (see Fig.XX). This approach was chosen due to the large operative band of the instrument since it is easier to process the signal once it is divided into sub-bands. Hereinafter each section of the instrument will be described and the characteristics provided.

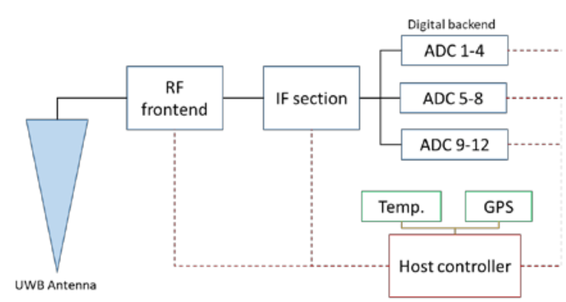

Fig. XX: Block diagram of the UWBRAD system. Measured signal is represented in black while red dashed lines represent the control ones.

A. Antenna

The antenna [9] designed for the UWB radiometer is a conical log spiral design including an internal balun feed (Fig. 1 left), conical antenna elements (Fig. 1 center), and a protective radome (Fig. 1 right). This kind of antenna provides near constant gain (thus footprint size) over the entire 0.5-2.0 GHz band. Also, the antenna has an aerodynamic shape which makes it possible to deploy it out of the bottom of the aircraft using a "periscope" system that allows for nadir measurements when the aircraft is in level flight. Fig. 2 plots measured values of the gain of the antenna, and shows values for the antenna used in the Greenland experiment. The average value is approximately 10 dB across the frequencies of interest (with a corresponding ~60 degree two-sided beamwidth) for right hand circular polarization (RHCP). For an aircraft operating at the nominal altitude of 500 m, the resulting circular footprint is ~0.6 km in diameter, requiring approximately 7.5 seconds to traverse at the nominal flight speed of 150 kts. Additional details regarding the antenna design can be found in [9].

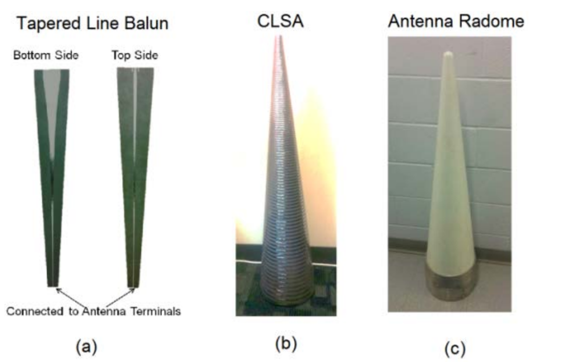

Fig. 1: images of a) internal balun board, b) conical log spiral antenna, and c) radome over antenna

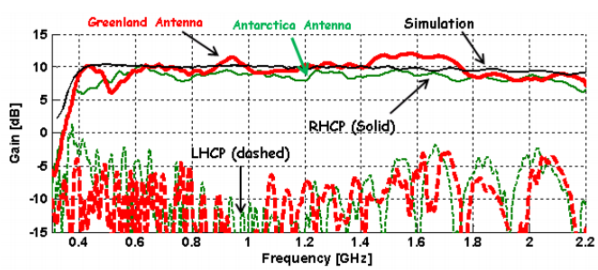

Fig. 2: Measured and Simulated UWBRAD Antenna gains (red lines for Greenland campaign)

B. RF frontend

Several configurations were considered in designing the RF frontend. A typical Dicke radiometer design was considered for UWBRAD, but the unavailability of components that operate over the entire bandwidth made the Dicke scheme unfeasible. Wide bandwidth 90° hybrids are available that met the project requirements, so a pseudo-correlation radiometer design was pursued, as shown in Fig. 3. In typical implementations of this design, two outputs (one approximately representing a reference load and the other the antenna) are observed to determine continuously the real-time parameters of the system and derive the observed brightness temperature. UWBRAD measures the two output signals sequentially (by toggling a phase shifter) to perform internal calibration.

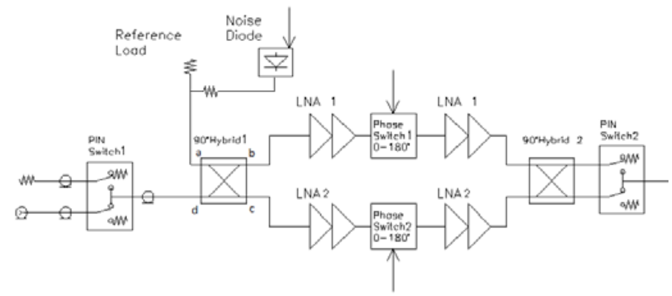

Fig. 3: Block diagram of UWBRAD RF frontend pseudo-correlation design

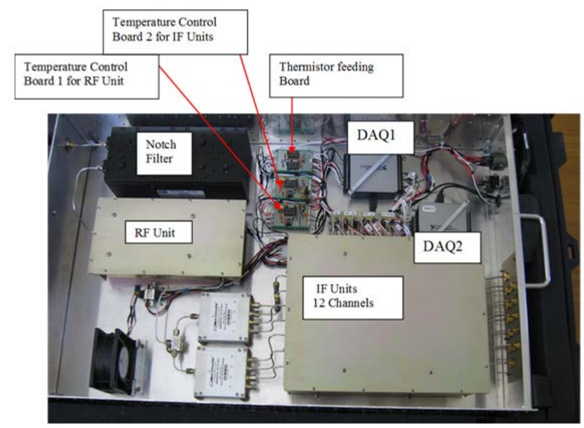

Fig. 4: Photo of UWBRAD RF and IF Units

The RF frontend unit (see Fig. 3) has two inputs to the first 90 degree quadrature hybrid: the antenna port (labeled 'd') and the reference port (labeled 'a'). The reference inputs include a 50 ohm termination at a known physical temperature combined with a switchable noise diode of known apparent temperature to allow a two point calibration approach. The antenna port has a switch (PIN Switch 1) that can be used to view a 50 ohm termination instead of the antenna to reduce potential interference when viewing the reference port. These signals then pass through the hybrid to two matched amplifier chains, each with an electronic 0°/180° phase shifter (Phase Switch 1 and 2). A second 90 degree hybrid is located at the output, with another switch (PIN Switch 2) used to select which output of the second hybrid to measure and which to terminate in 50 ohms.

In the UWBRAD frontend, the four switches and the noise diode condition give the possibility of 32 (2^5) states to be observed. In the case of perfect hybrid XX are redundant and only XX are necessary for the radiometer calibration. However, given the accuracy required for UWBRAD (<1K), at least XX are necessary. The combination of the noise diode and PIN Switch 1 states define the four inputs into the system: antenna plus reference, antenna plus noise diode, antenna terminated plus reference, and antenna terminated plus noise diode. Since the hybrids are not ideal, each of the two outputs of the second hybrid are the sum of a dominant and a minor signal associated with each of the inputs (explored further in Section III): one output is reference dominant/antenna minor and the other is antenna dominant/reference minor. The minor terms are due to the non perfect shift of the 90deg hybrids, that makes the signals flowing through them to not perfectly sum and cancel each another. The remaining three switches all have the effect of selecting which output is being viewed. The phase shifters do so by changing the electrical phase of one path, changing the interference pattern such that what was destructive interference becomes constructive and vice versa. PIN Switch 2 does so by observing the other output of the second hybrid. Activating two of these switches at the same time simply toggles twice, leaving the original combination of output signals (output is an XOR of the three switches). During calibration testing, no clear benefit emerged for using any particular combination of these three switches, so Phase Switch 1 was chosen to toggle between the outputs, and Phase Switch 2 and PIN Switch 2 were not switched in the calibration process.

C. IF section

After the RF frontend, the signal is divided into ten ~81 MHz bandwidth channels and two ~60 MHz channels as shown in Figs. 5-6. Bandpass filters are used on each channel to help prevent cross-talk interferences. A thirteenth channel was originally planned, but was removed due to a powerful transmitter on the aircraft around 1000 MHz (which the notch filter identified in Fig. 4 helps mitigate). Seven local oscillators (LO) are used to downconvert the twelve channels to a common 180 MHz IF frequency for analog-to-digital (A/D) conversion by the digital backend (operating in the first Nyquist zone of the A/D cards). Ten of the twelve channels are paired in an upper and lower sideband configuration with a common LO. The remaining two channels have a dedicated LO. After downconversion, each channel has an antialiasing bandpass filter before being sent on to the digital backend.

D. Backend

The digital backend is composed of four computers: one host computer and three analog-to-digital conversion clients. The host computer is responsible for acquiring ancillary data (such as temperature and location information) and triggers acquisition of data on the three client computers. The client computers wait for a signal from the host to acquire data, then process and store the data. The client computers each hold two AlazarTech analog-to-digital conversion cards that convert two channels per card. These cards operate at 250 MS/s at 16 bits per sample. The client computers also each hold eight 4 TB hard drives for data storage. Each channel has a dedicated hard drive with automatic backup to a second drive (RAID 1 configuration).

Each acquisition performed by the digital backend is 100 msec long. Storing all of the raw samples would require an excessive amount of storage space, so in normal operations the raw data is processed into “medium rate” and “low rate” data for storage. Medium rate data stores time domain power in 100 x 1 msec intervals, and also uses Fast Fourier Transforms (FFT) to create a 512 bin spectrogram for each 1 msec interval, resulting in a 512 x 100 point spectrogram matrix in the medium rate data product. The kurtosis of each 1 msec interval as well as the subband kurtosis of each frequency bin are calculated and also stored in medium rate files. RFI algorithms are run onboard (fullband kurtosis, pulse blanking, subband kurtosis, cross frequency) and the flags for each algorithm are stored to complete the medium rate data product. The low rate data product integrates over the entire channel before and after RFI algorithms are applied and stores these two numbers as well as the total percentage of data flagged as RFI.

It is necessary to acquire several different states to achieve a calibrated brightness temperature (details in section III). The time required to acquire, process, and store all of the states needed for a single brightness temperature product averages around 2 seconds, so that the final duty cycle of UWBRAD antenna measurements is approximately 5%. This is not a problem for UWBRAD as ample integration time is available per footprint. It would be possible to increase the duty cycle by performing extra antenna measurements between internal calibration state measurements, but this has not been pursued at this time.

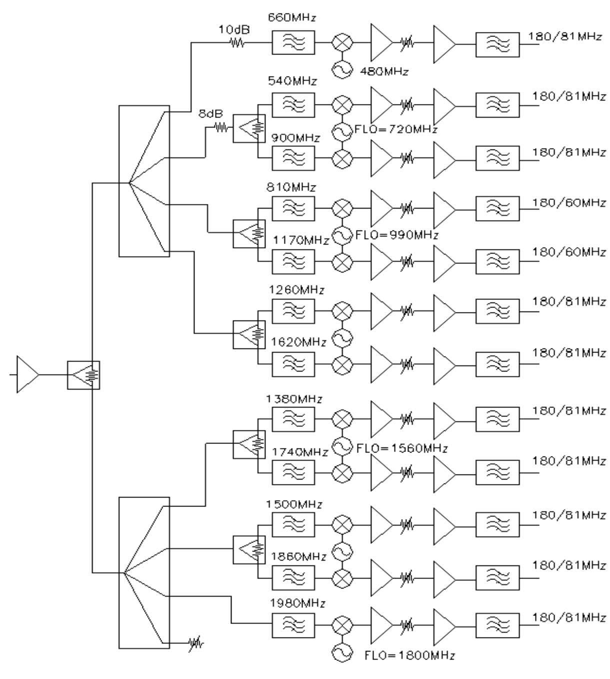

Fig. 5: Block diagram of UWBRAD IF units

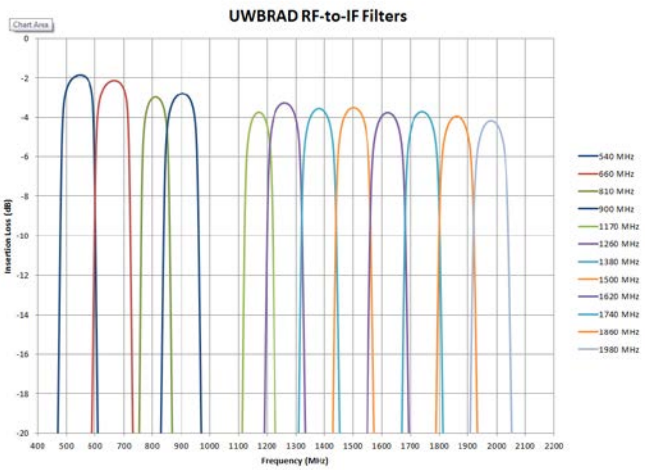

Fig. 6: Filter responses in IF section

III. CALIBRATION

To determine a calibration procedure for the radiometer, a mathematical formulation for the signals present at the output of the RF unit is needed. A summary of the voltage signals of interest for the derivation is provided in Table 1. Using these variables, the complex voltages of the front end can be summarized in the form of equations (1) and (2).

$$V^0 = V_R\left(H_{1,ca}G_2H_{2,cd} + H_{1,ba}G_1H_{2,ca}\right) + V_A\left(H_{1,cd}G_2H_{2,cd} + H_{1,bd}G_1H_{2,ca}\right) + V_{N1}G_1H_{2,ca} + V_{N2}G_2H_{2,cd} \quad \textbf{(1)}$$

$$V^{180} = V_R\left(H_{1,ca}G_2H_{2,cd} - H_{1,ba}G_1H_{2,ca}\right) + V_A\left(H_{1,cd}G_2H_{2,cd} - H_{1,bd}G_1H_{2,ca}\right) + V_{N1}G_1H_{2,ca} + V_{N2}G_2H_{2,cd} \quad \textbf{(2)}$$

Table 1: Voltage Variables

V^X	Output voltage when Phase Switch 1 is in X degree position
V_A	Voltage at the antenna input port of the radiometer
V_R	Voltage of the reference load input port of the radiometer
G_1	Voltage gain (magnitude only) of LNA path 1
G_2	Voltage gain (magnitude only) of LNA path 2
V_{N1}	Added noise voltage from active circuits in path 1
V_{N2}	Added noise voltage from active circuits in path 2
$H_{x,zy}$	Transmission coefficient of hybrid X from port y to port z. Includes 90 degree phase shift for bd and ca paths, 0 degrees for cd and ba

In equations (1) and (2), the phases of the H terms constructively and destructively interfere such that V^0 will have a large gain term (approximately 2G where G is the gain of one amplifier) for V_R and a term near 0 for V_A. When the phase switch is in the 180 degree position, the interference pattern alternates such that V_R will now have a small gain and V_A will have the large gain.

Calculating the power of the outputs (computing the amplitude squared of the signal) causes cross products of the various terms to appear. Since these are all independent random noise signals, integrating over time will cause these cross products to vanish, leaving the following equations to describe the system (variables defined in Table 2):

$$P^0 = C_R^0 T_R + C_A^0 T_A + N \quad \textbf{(3)}$$

$$P^{180} = C_R^{180} T_R + C_A^{180} T_A + N \quad \textbf{(4)}$$

Table 2: Power Variables

P^X	Output power when Phase Switch 1 is in X degree position
$C^X_{R/A}$	Gain coefficient (W/K) for reference (R) or antenna (A) path when Phase Switch 1 is at X degrees.
$T_{R/A}$	Noise temperature of reference (R) or antenna (A) input port
N	Added noise power in system due to active circuits

The net result is that the output has a dominant term proportional to one input signal, a smaller term proportional to the other input signal, and an offset from the noise added due to active circuits (LNA and phase shifter). Toggling a phase switch was chosen instead of using PIN Switch 2 so that the added noise in the system followed the same path through the output hybrid. Assuming the phase shifter's added noise component remains constant with its setting, this would result in the same N term for all measurements. Lab tests showed that using Phase Switch 2 or PIN Switch 2 instead is similarly effective, so the "0" and "180" states can be used with any switch or combination of switches without losing generality.

There are now four radiometer states that can be observed: dominant reference signal with noise diode on/off, and dominant antenna signal with noise diode on/off. Using these states, the calibration sequence to determine the temperature at the antenna input port is:

1. Measure both phase switch positions with the noise diode off, then subtract the results:
$$(C_R^0 T_R + C_A^0 T_A + N) - (C_R^{180} T_R + C_A^{180} T_A + N) = (C_R^0 - C_R^{180})T_R + (C_A^0 - C_A^{180})T_A \quad \textbf{(A)}$$

2. Measure both phase switch positions with the noise diode on, then subtract the results:
$$(C_R^0[T_R + T_D] + C_A^0 T_A + N) - (C_R^{180}[T_R + T_D] + C_A^{180} T_A + N) = (C_R^0 - C_R^{180})[T_R + T_D] + (C_A^0 - C_A^{180})T_A \quad \textbf{(B)}$$

3. Subtract (A) from (B) to obtain

$$(C_R^0 - C_R^{180})T_D$$

4. Define

$$Q = \frac{A}{B-A} = \frac{T_R}{T_D} + \frac{T_A}{T_D} f$$

where

$$f = \frac{(C_A^0 - C_A^{180})}{(C_R^0 - C_R^{180})}$$

With T_R(reference load physical temperature measured by a thermistor), T_D (excess temperature due to the noise diode, derived through lab testing), and f (derived through lab testing) defined, T_A can be solved for from the four state measurements. This process assumes that T_D and f are stable parameters once calibrated. Laboratory and campaign tests confirm this assumption so that a stable calibration of UWBRAD is achieved.

IV. Lab Results

Laboratory testing was used to determine the excess brightness of the noise diode (T_D) and the gain ratio parameter *f*. A digital step attenuator was attached to the radiometer input and connected to a cable terminated in a matched 50 ohm load, which was placed in liquid nitrogen (temperature of 77.15 K). The temperature of the room and the S parameters of the cable and step attenuator were measured to determine the truth input temperature at the radiometer input for each attenuator value. The entire system was placed in a thermal chamber and the attenuators cycled through their values while the chamber temperature ranged from 0 to 30 °C. This test was performed for a continuous 24 hour period to derive the calibration of the radiometer. Repeated liquid nitrogen tests performed at ambient temperatures before the campaign showed similar results, suggesting a stable noise diode and system performance.

The Q parameter was calculated from the various state powers recorded and line fit for each frequency bin to determine the noise diode temperature and *f* parameter. The results versus frequency are shown in Fig. 7. With these two parameters derived, the antenna temperature was calculated using the new values.

For each channel, the gain at the band edges eventually reduces to the point that the ADC does not have the precision to retrieve antenna temperatures accurately. Once the retrieval error of a frequency bin exceeds a certain threshold, these band edges are removed from the calculation to reduce the root mean square error (RMSE) of the retrieved temperatures. After performing RFI processing and integrating over frequency for each of the 12 channels, the RMSE from the predicted input temperature for the channels ranged from 0.28-0.48 K for a 100 msec integration period, detailed in the third column of Table 3, and followed by the resulting system temperature determined from this value. The second column of Table 3 shows the average bandwidth of the channel during LN2 testing after removal of band edges and RFI processing (some internal spurious signals can be detected and flagged, reducing the bandwidth). The goal was an error of 1 K for each channel, so these laboratory tests confirm that the radiometer met the desired performance for all 12 channels. Fig. 8 shows a spectrogram example of one channel (channel 7, 1380 MHz center frequency) and the error between the retrieved temperature and predicted input temperature. The degradation of the band edges can be seen below 1320 MHz and above 1430 MHz, and some small internal interference can be seen around 1335 and 1395 MHz. These bins are either removed manually (in the case of band edges) or by RFI flagging (for interferers) before calculating final temperatures.

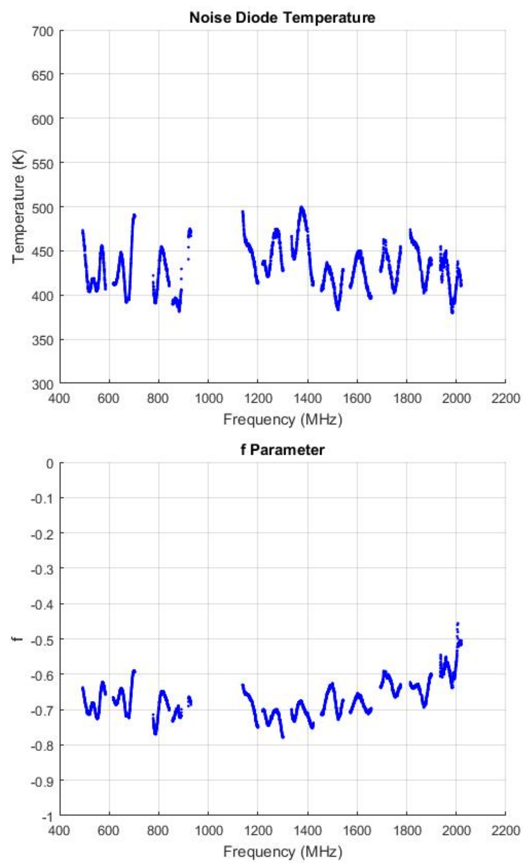

Fig. 7: Calibration results for noise diode temperature (top) and *f* gain ratio parameter (bottom)

Table 3: UWBRAD channel performance at ambient temperature

Channel	Center Frequency (MHz)	Average Bandwidth (MHz)	RMSE (K)	T_{sys} (K)
1	540	86	0.33	684
2	660	90	0.34	764
3	810	75	0.48	665
4	900	102	0.35	784
5	1170	78	0.31	652
6	1260	105	0.29	679
7	1380	104	0.34	817
8	1500	108	0.28	701
9	1620	106	0.33	758
10	1740	98	0.31	646
11	1860	102	0.35	884
12	1980	83	0.44	1013

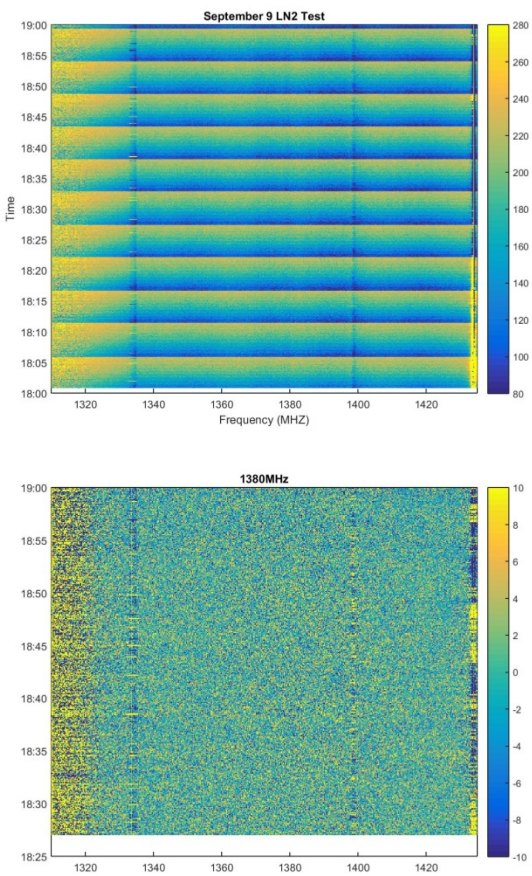

Fig. 8: LN2 test retrieval spectrogram for 1380 MHz channel as the input brightness temperatures are cycled over a range of values in periodic fashion (top) and difference between calibrated and known input temperatures (bottom)

V. RFI ALGORITHMS

Given UWBRAD's wide bandwidth operation in unprotected bands, many types of RFI were expected to be encountered. RFI detection algorithms working in the time, frequency and statistics domains were therefore used for UWBRAD, following a process similar to that used for the SMAP microwave radiometer [10]. As with SMAP, UWBRAD produces both "fullband" (i.e. time domain powers representing the entire bandwidth in a given channel) and "sub-band" (spectrograms of the integrated power in 512 frequency channels at 1 msec time resolution) products. UWBRAD applies its time domain algorithms first (Level 1 Processing) using fullband products to flag short pulsed and non-Gaussian RFI. Then sub-band algorithms are applied (Level 2 Processing) to flag any frequency dependent RFI.

In Level 1 Processing, each 100 msec acquisition is divided into 100 x 1 msec intervals, and the kurtosis and integrated power for each of these intervals are computed. The fullband kurtosis algorithm is applied first and operates on-board in real-time. The fullband kurtosis algorithm flags any 1 msec intervals having a kurtosis value outside a user defined range as RFI.

The pulse blanking algorithm also operates in real time, but was recomputed for this campaign in post-processing in order to optimize performance. The algorithm used is based on the Median Absolute Deviation method described in Peck [11] and operates on the 512 x 100 point spectrogram of the received power. After fullband kurtosis flagged intervals are discarded, the pulse blanking algorithm calculates the median value of the power in the remaining 1 msec intervals for each frequency bin. The median value of each bin is subtracted from the spectrogram, resulting in a signal centered near zero for most samples. The median of the absolute value of this deviation is then calculated. Any time intervals for which the power deviation exceeds 4 times the median absolute deviation are then flagged as pulses. This results in a false alarm rate (FAR) of approximately 1% for each frequency bin. The final Level 1 product is created by integrating the UWBRAD spectrogram over the 100 msec measurement interval both including (unmitigated) and excluding (mitigated) 1 msec intervals flagged by the kurtosis and pulse blanking algorithms, representing power in 512 frequency bins at 100 msec time resolution.

Fig. 9 (in Section VI) shows the spectrograms of observed brightness temperatures during the transit flight of the campaign before and after each stage of RFI processing. The third image in each figure shows the Level 1 product for the scenes after application of the fullband kurtosis and pulse detection algorithms. Several examples of pulsed RFI are removed, and in some cases, entire channels are flagged as RFI (particularly early on, near population centers Calgary and Edmonton).

The processing to Level 1 operates directly on the recorded powers. At this point, the data is calibrated using the procedures described in Section III to obtain antenna temperatures resolved into 512 frequency bins (over the full measured 125 MHz frequency range including band edges) at

100 msec time resolution. The cross frequency algorithm is now applied for each 100 msec interval to identify anomalous frequency bins. The cross frequency algorithm is similar to the algorithm presented in Guner [12]. However, rather than using the mean of the lowest 85% of antenna temperatures in setting detection thresholds, it uses the median value across frequency of the antenna temperature instead. Thresholds for this detector are set at 15 K for an average FAR of approximately 1%. The fourth image of Fig. 9 provides the Level 2 product after application of the cross frequency algorithm to the Level 1 product.

These algorithms flag most of the clearly visible RFI, but there are still some brightness anomalies visible. Sub-band kurtosis was calculated and may be useful for additional RFI flagging, but it was not used on this campaign as it appeared to have a high FAR due to the impact of short pulsed interference. Additional pulse blanking algorithms can also be subsequently applied in post-processing (on an as-needed basis) over a time period of 1 hour at 100 msec time resolution for the integrated power of each channel to help mitigate these additional anomalies.

VI. Field Results

A field campaign for UWBRAD was conducted from September 12-15, 2016. The system was installed on a DC-3 Basler aircraft supplied by Kenn Borek Airlines and was operated on a transit flight from Calgary to Thule Airbase, Greenland and then on a flight from Thule airbase in Greenland. A photo of the flight configuration is presented in Fig. 13.

Fig. 9 shows the path of the transit flight and spectrogram results from Calgary to Cambridge Bay, Canada on September 12th, 2016. Fig. 10 illustrates the campaign flight path and spectrogram results out of Thule on Sept 15th, 2016. Each figure also includes a sample of the time series that includes water and land observations (integrated over the entire 1500 MHz bandwidth of UWBRAD). The region observed in Fig. 10 includes sea scenes, “rock” regions near the coast, as well as portions of the Greenland ice sheet where ablation, wet snow, percolation, and dry snow, respectively, are expected to be dominant processes influencing the thermal emission of the upper portion of the ice sheet. Flights over water scenes were conducted on both flights for external calibration. Estimates of water temperature and salinity are used to derive the expected brightness temperature of the scene. This information is used to determine the losses of the antenna and cable at the input of the radiometer to convert retrieved antenna temperatures into scene brightness. The brightness temperatures in these figures are reported at 244 kHz (125 MHz/512 bins) x 100 msec resolution (Note: These figures include the band edges of each channel to

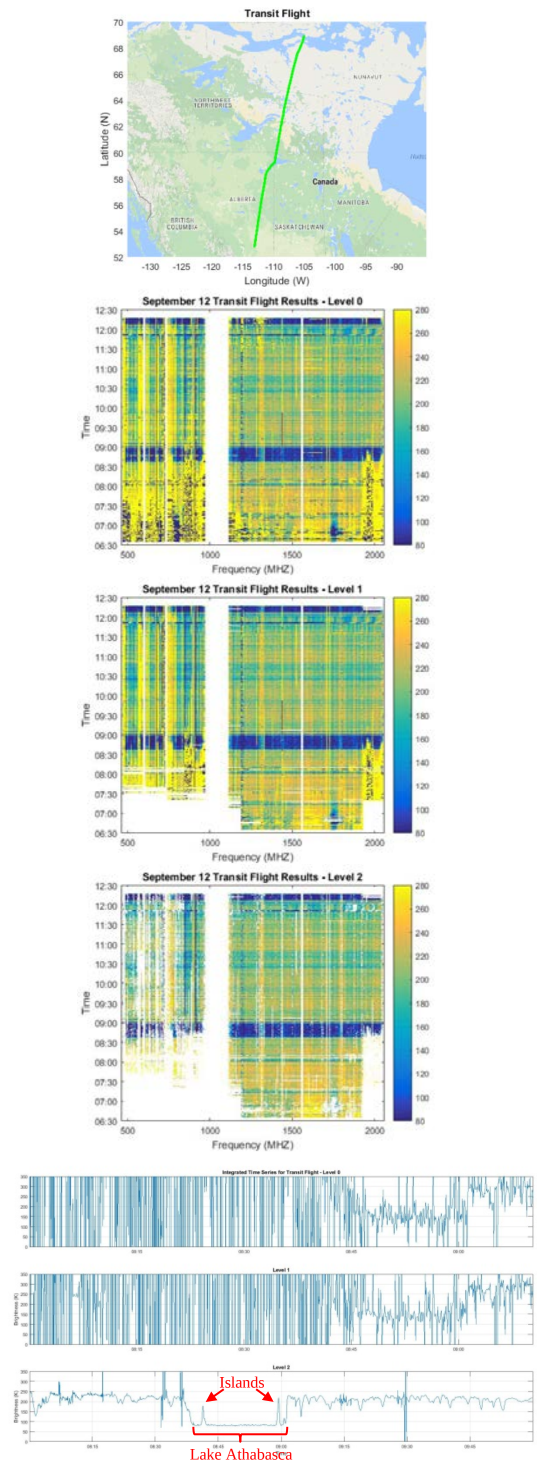

Fig. 9: Flight line for transit path data (top) and level 0 (second), level 1 (third), and level 2 (fourth) brightness spectrograms. Integrated time series sample (bottom)

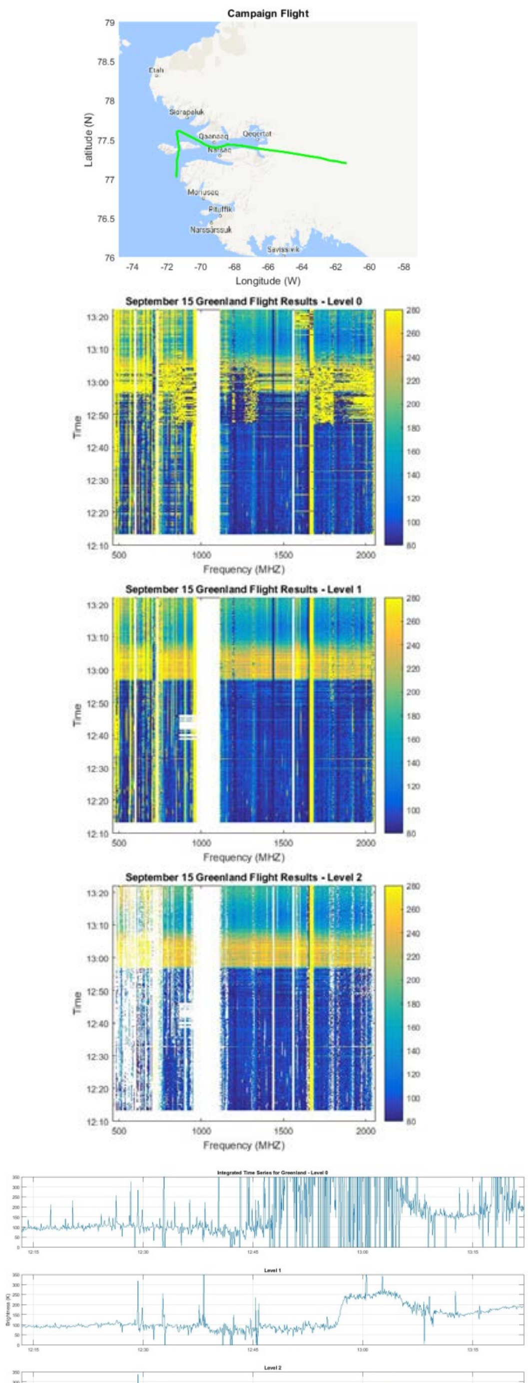

Fig. 10: Flight line for Greenland data (top) and level 0 (second), level 1 (third), and level 2 (fourth) brightness spectrograms. Integrated time series sample (bottom)

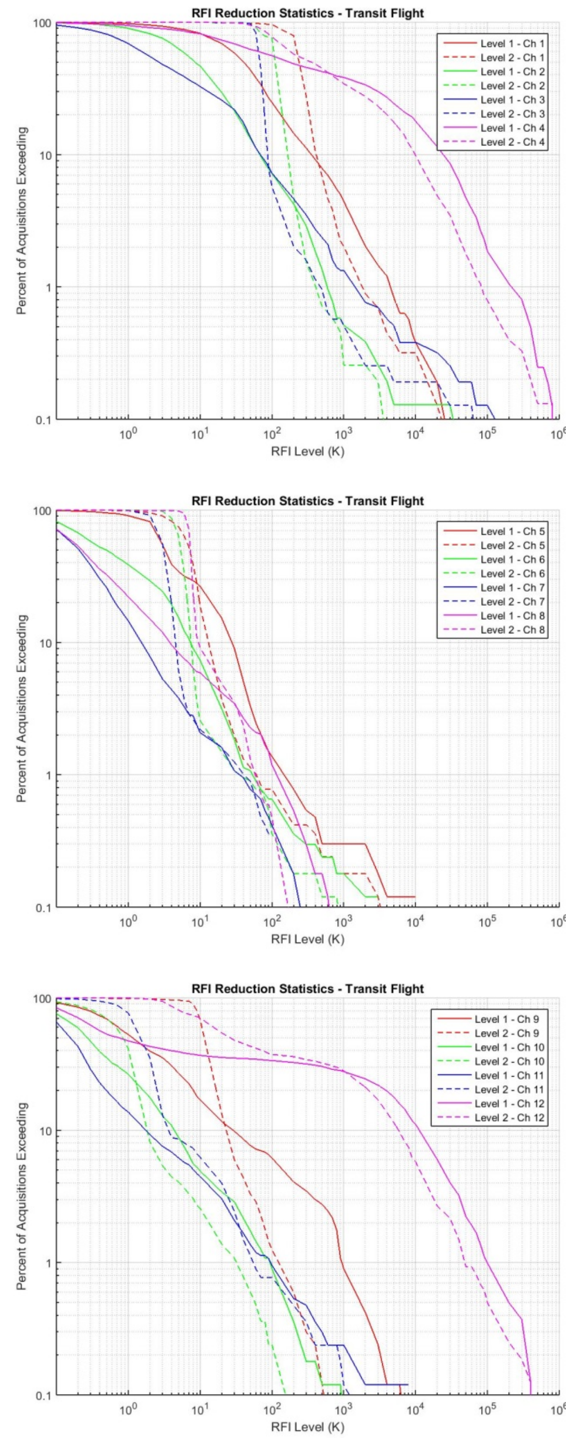

Fig. 11: RFI encountered during transit flight for channels 1 through 4 (top), 4 through 8 (middle), and 9 through 12 (bottom)

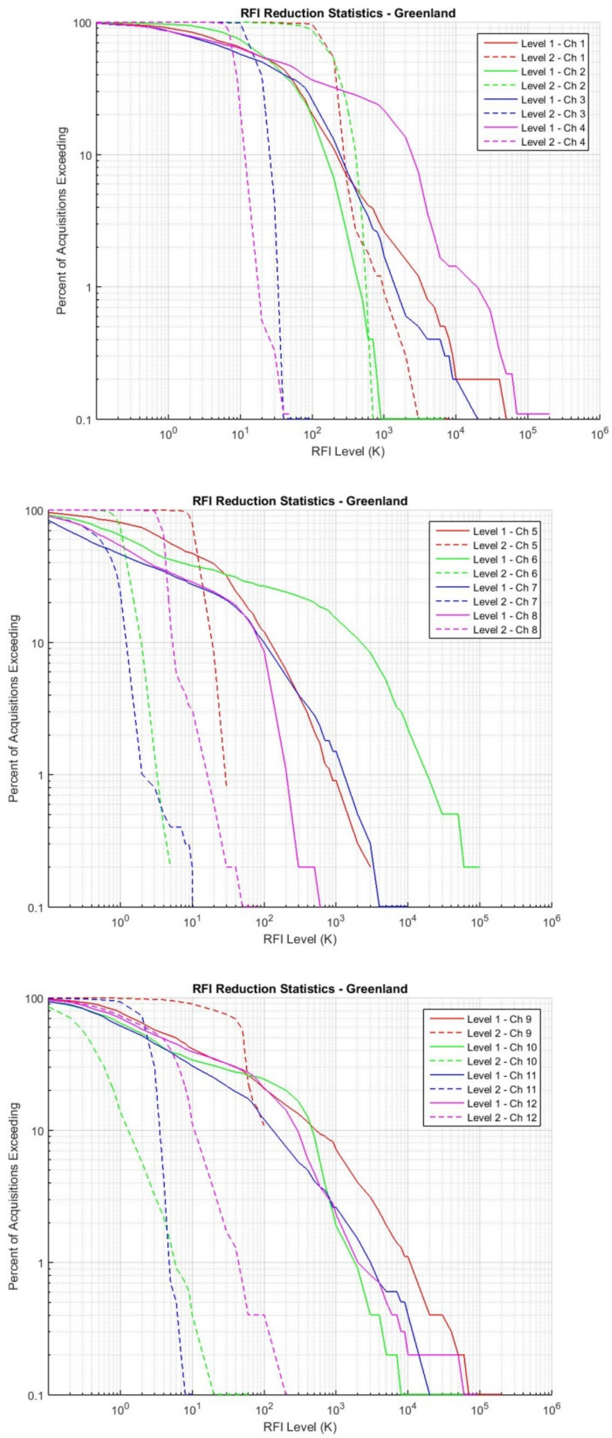

Fig. 12: RFI encountered during Greenland flight for channels 1 through 4 (top), 4 through 8 (middle), and 9 through 12 (bottom)

make the image clearer. In some cases this appears as a brightness anomaly localized in frequency). The time series plots in the lower portions of Figs. 9 and 10, which are integrated over all available UWBRAD measurements from 0.5-2 GHz, illustrate values obtained prior to any RFI processing, after Level 1 processing, and after Level 2 processing, respectively. The significantly smoother curves resulting after both processing levels appear to correspond to geophysical expectations, although some residual RFI contributions remain in this full spectrum product that are reduced in individual UWBRAD channels. The strong presence of pulsed sources that are effectively filtered by the Level 1 processor is also apparent in the Greenland flight results of Fig. 10.

To illustrate the RFI encountered during these flights, complementary cumulative distribution functions (ccdf's) of the magnitude of RFI encountered in each channel are presented in Fig. 11 (transit flight) and Fig. 12 (Greenland flight). The twelve channels have been distributed among three different graphs for clarity. The x-axis represents the difference in brightness temperature between one RFI mitigation level and the previous level; i.e., a "Level 1" plot indicates the difference in integrated brightness magnitude between the Level 0 raw data and the Level 1 RFI mitigated product, and the "Level 2" plot is the difference between the Level 1 and Level 2 mitigated products. The y-axis shows the percentage of acquisitions where the brightness temperature difference exceeded the RFI magnitude on the x-axis. Level 0 to Level 1 plots are solid lines, and Level 1 to Level 2 are dashed.

The figures show that a wide range of RFI sources were encountered, with magnitudes ranging up to 1 million K or more. This is not unexpected as no channel was operating in a protected band, so some very strong signals were encountered. Examples of amplifier saturation in the RF unit could also be seen, where a strong interferer in one channel caused a reduction in gain across all channels. In many cases, nearly 100% of the acquisitions for a channel show some level of RFI. This is due to a combination of false alarms in the flagging algorithm and persistent internal RFI sources (particularly for Level 1 to Level 2 processing) that are not separated from external contributions in these analyses.

Comparing all of the channels, it is apparent that RFI below 1 GHz (channels 1 through 4) is generally more frequent and more powerful than at other frequencies. RFI in channel 12 was prevalent near the population centers in Canada, but more in line with the other channels in Greenland and low population areas. Both pulsed and more continuous RFI contributions are apparent, with pulsed RFI representing a larger portion of the sources observed in the Greenland flight. Low-level RFI is common in all channels, some of it likely generated on-board the aircraft (either from the equipment or the aircraft itself).

Fig. 13: Flight configuration of UWBRAD

The UWBRAD team is also investigating forward modeling of the full 0.5-2 GHz measured data for the differing portions of the Greenland ice sheet observed. A more detailed analysis of this work can be found in Jezek [8]. The UWBRAD flight plan was intended to pass over multiple core sites in the central Greenland ice sheet and end in Sondrestrom, Greenland. Unfortunately, the RF frontend unit experienced two failures in the campaign: one shortly after takeoff from Cambridge Bay on the transit flight to Greenland, and a second failure on the backup unit after ~90 minutes of collecting data in Greenland. Both failures showed damage to the initial amplifiers in the front end chain. It was determined that the damage appeared to be caused by an excessively high input signal. This may have been caused by a buildup and discharge of static electricity in the antenna or a strong signal from one of several high power radars in the area (airports, North Warning System, Ballistic Missile Early Warning System). Precautions will be made on future campaigns to include power limiters and ESD diodes on the input to protect against ESD and strong RFI environments. A second campaign to achieve observations of the central portion of the Greenland ice sheet is planned for September 2017.

VII. Conclusion

UWBRAD has shown through lab tests and a field campaign that it is capable of making stable and accurate radiometric measurements over the 500-2000 MHz frequency range in the presence of RFI. The UWBRAD team is still analyzing the data that the instrument collected from the field campaign, and also making improvements to the robustness of the system in preparation for an upcoming second campaign in September 2017. Access to wideband brightness temperatures outside of protected science bands will be invaluable for the future of ice sheet subsurface temperature analysis, and the team is optimistic that UWBRAD will be able to provide this information.

VIII. References

[1] Jezek, K. C., J. T. Johnson, M. R. Drinkwater, G. Macelloni, L. Tsang, M. Aksoy, and M. Durand, “Radiometric approach for estimating relative change in intra-glacier average temperature,” IEEE Trans. Geosc. Rem. Sens., vol. 53, pp. 134-143, 2015.

[2] M. Aksoy, J. T. Johnson, K. C. Jezek, M. Durand, M. R. Drinkwater, G. Macelloni, and L. Tsang, ``An examination of multi-frequency microwave radiometry for probing subsurface ice sheet temperatures,'‘ IGARSS, 2014.

[3] Brogioni, M., S. Pettinato, F. Montomoli, K. Jezek, and G. Macelloni, “Simulating multi-frequency ground based radiometric measurements at DOME-C Antarctica,” IEEE JSTARS, vol. 8, pp. 4405-4417, 2015.

[4] Tan, S., M. Aksoy, M. Brogioni, G. Macelloni, M. Durand, K. Jezek, T. Wang, L. Tsang, J. T. Johnson, M. Drinkwater, L. Brucker, “Physical models of layered polar firn brightness temperatures from 0.5-2 GHz,” ,” IEEE JSTARS, vol. 8, pp. 3681-3691, 2015.

[5] G. Picard, L. Brucker, A. Roy, F. Dupont, M. Fily, and A. Royer, “Simulation of the microwave emission of multi-layered snowpacks using the dense media radiative transfer theory: the DMRT-ML model,” Geosci. Model Dev. Discuss., 5, 3647-3694, 2012.

[6] A. Bringer, et al, ``An examination of models for predicting the 0.5-2 GHz brightness temperature of ice sheets,'‘ IGARSS15.

[7] T. Wang, L. Tsang, J. T. Johnson, K. C. Jezek, and S. Tan, “Partially coherent model for the microwave brightness temperature of layered snow firn with density variations and interface roughness,” IGARSS, 2015

[8] K. Jezek, J. Johnson, et al " 500-2000 MHz Brightness-Temperature Spectra of the Northwestern Greenland Ice Sheet”, submitted to TGARS 2017.

[9] D. Belgiovane, C. Chen, J. Johnson “Conical log spiral antenna development for the UWBRAD ice sheet internal temperature sensing”. 978-1-5090-2886-3/16/ ©2016 IEEE

[10] J. Piepmeier, J. Johnson, P. Mohammed, et al. “Radio-Frequency Interference Mitigation for the Soil Moisture Active Passive Microwave Radiometer”, IEEE Trans. Geosc. Rem. Sens., vol. 52, no. 1, Jan 2014

[11] L.W. Peck, D.E. Fenech “SERPent: Automated reduction and RFI-mitigation software for e-MERLIN,” Astronomy and Computing, Vol. 2, August 2013, pp.57

[12] Guner, B., N. Niamsuwan, and J. T. Johnson, 2007. “Time and frequency blanking for RFI mitigation

in microwave radiometry", IEEE Trans. Geosc. Rem. Sens., vol. 45, pp. 3672—3679.